Hindawi
International Journal of Aerospace Engineering
Volume 2022, Article ID 7881535, 20 pages
https://doi.org/10.1155/2022/7881535

Research Article

Nonsingular Global Fast Terminal Sliding Mode Control with Extended State Observer for Contact Force Regulation in Aerial Manipulator

Lirui Shen, Pengjun Mao, Qian Fang, and Jun Wang

School of Mechanical and Electrical Engineering, Henan University of Science and Technology, Luoyang 471000, China

Correspondence should be addressed to Pengjun Mao; mpj@haust.edu.cn

Received 9 June 2022; Revised 28 September 2022; Accepted 30 September 2022; Published 11 November 2022

Academic Editor: Francisco Ronay Lopez Estrada

The aerial manipulator is a novel flying robot consisting of an unmanned aerial vehicle (UAV) and a multi-degree-of-freedom (DoF) robotic arm. It can actively interact with the environment to conduct dangerous or inaccessible tasks for humans. In this paper, we propose a composite control scheme considering force and position for the aerial manipulator to operate in steady contact with the environment when influenced by external disturbances. First, a contact force control method without employing the force sensor is obtained on the mechanical relationship of the system's contact with the environment. Second, we regard the system's internal coupling and external disturbance as lumped disturbances and design an extended state observer (ESO) to estimate them. Combined with the disturbance estimation and the nonsingular global fast sliding mode algorithm, a controller derived from the Lyapunov theory is proposed. Finally, we compare the proposed controller with the other four controllers through simulations and actual flight experiments. The results show that the proposed controller can effectively restrain disturbances, reduce convergence time, and guarantee steady contact under external disturbances.

1. Introduction

UAVs have played an essential role in many fields in recent years, such as plant protection [1], rescue [2, 3], and security [4]. However, UAVs' inability to interact with the environment is an important reason that limits their development. In order to complete aerial interaction tasks, researchers have integrated robotic arms with UAVs, which are called aerial manipulators, for use such as in visual inspection [5], aerial maintenance [6], and glass cleaning [7]. The operating ability of the aerial manipulator has expanded the scope of UAVs' application and has excellent potential for development.

Since the aerial manipulator is an underactuated system with strong coupling, the steady flight of the UAV and the accurate operation of the manipulator are essential for an aerial manipulator to complete manipulation tasks. Hence, the aerial manipulator system control has attracted considerable attention. A variety of control methods has been applied to the aerial manipulator, such as impedance control [8, 9], back-stepping control [10, 11], model predictive control [12–14], adaptive control [15–17], and sliding mode control [18–22]. A controller based on impedance control was developed and applied to the aerial manipulator for interference rejection caused by the robotic arm motion [9]. The visual servo problem was formulated as a stochastic model predictive control framework for the aerial manipulator with a three-DoF manipulator to grasp objects [12]. An adaptive controller was designed for an aerial manipulator system with a two-DoF robotic arm to transport an unknown load, which could estimate the load's parameters online and track the desired trajectory [16]. A sliding mode controller was developed for an aerial manipulator with a three-DoF robotic arm to grasp and transport objects [19]. An adaptive integral-type terminal sliding mode approach was proposed for the attitude and position tracking control of a quadrotor UAV subject to model uncertainties and external disturbances [22]. The above studies show that the system control performance on interaction with the environment can be enhanced by improving the controller. However, these operations are

conducted with the UAV in a free flight state. When the system contacts the environment, a contact force will be generated between them. Although its presence and impact are usually overlooked, the existence of contact force will inevitably increase the instability of the system and the vibration caused by the increased hardware load of the body, leading to increased errors and reduced efficiency. Therefore, the stable contact between the aerial manipulator and the environment has become a problem to be solved.

So far, numerous studies are on contact force control for the aerial manipulator interacting with the environment, and some of them are about the constant contact force control when the aerial manipulator interacts with the environment. A controller based on the impedance control algorithm was developed for the aerial manipulator with a one-DoF robotic arm for continuous contact with the environment [23]. A force and position hybrid control framework was used to control the aerial manipulator to continuously contact the environment and track the desired trajectory [24]. An aerial manipulator system based on an octarotor was designed to measure the bridge life by applying continuous contact force on bridges [25]. The above research shows that the aerial manipulator can maintain a constant contact force when interacting with the environment, but these operations were conducted without considering external disturbances. There is various kinds of environmental interference in practical applications, such as gusty wind. Wind disturbance will seriously affect the aerial manipulator system's stability because the UAV's driving force comes from aerodynamic force. Therefore, robustness against wind disturbance is crucial for the aerial manipulator system.

This paper offers a force/position control scheme for the motion problem of the aerial manipulator, which is aimed at ensuring that the aerial manipulator can reliably contact the external environment under external disturbance influence while maintaining a particular contact force. The space in which the aerial manipulator performs the contact operation is divided into the contact space orthogonal to the contact surface and the free space parallel to the contact surface. Force control and motion control are performed in these two spaces, respectively. In the contact space, since the aerial manipulator requires continuous contact with the environment, the controller should be designed first to ensure the system's stability. Then, we obtain the control method through the analysis of the mechanical relationship to realize the contact force control. For position control in the free space, it is achieved by the trajectory tracking of the controller. In addition, in order to compensate for disturbances for the controller, we treat the external disturbance and the internal coupling of the system as lumped disturbances, and an extended state observer is designed to estimate them. Based on the sliding mode control algorithm and extended state observer technology, we propose a composite control scheme for an aerial manipulator in contact with the environment.

Compared with previous related works, the main innovations of this paper are as follows:

(1) By introducing and improving the nonsingular global fast terminal sliding mode function to enhance the robustness and convergence of the system

(2) The estimation and compensation of the extended state observer to lumped disturbances significantly enhance the closed-loop system's antidisturbance capability

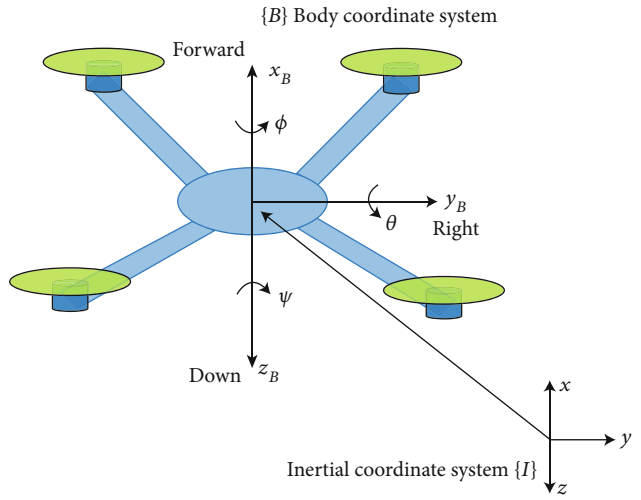

Figure 1: The coordinate system of the quadrotor UAV system.

The rest of this paper is organized as follows. In Section 2, the kinematics and dynamics of the aerial manipulator are introduced, and the force control method is obtained by parsing the dynamic relationship. After that, the control scheme of the aerial manipulator and the system stability proof are given in Section 3. Then, a comparison simulation with other control schemes is conducted in Section 4. Next, two sets of actual flight comparative experiments are carried out in Section 5. Finally, conclusions are presented in Section 6.

2. System Modeling and Mechanical Relationship

The multirotor UAV system is underactuated with strong coupling characteristics of multiple inputs and outputs. The inertial coordinate system $\{I\}$ and the body coordinate system $\{B\}$ are as shown in Figure 1.

$\{\phi, \theta, \psi\}$ represent the roll angle, pitch angle, and yaw angle of the body in the inertial coordinate system, respectively; $\{x, y, z\}$ represent the body's position in the inertial coordinate system. The translational dynamics and attitude dynamics models of the system in the inertial system are

$$\begin{aligned}
\ddot{x} &= \frac{U_1}{m}\left(C_\phi S_\theta C_\psi + S_\phi S_\psi\right) - \frac{k_t \dot{x}}{m} + \frac{D_x}{m},\\
\ddot{y} &= \frac{U_1}{m}\left(C_\phi S_\theta S_\psi - S_\phi C_\psi\right) - \frac{k_t \dot{y}}{m} + \frac{D_y}{m},\\
\ddot{z} &= \frac{U_1}{m} C_\phi C_\theta - g - \frac{k_t \dot{z}}{m} + \frac{D_z}{m},
\end{aligned} \tag{1}$$

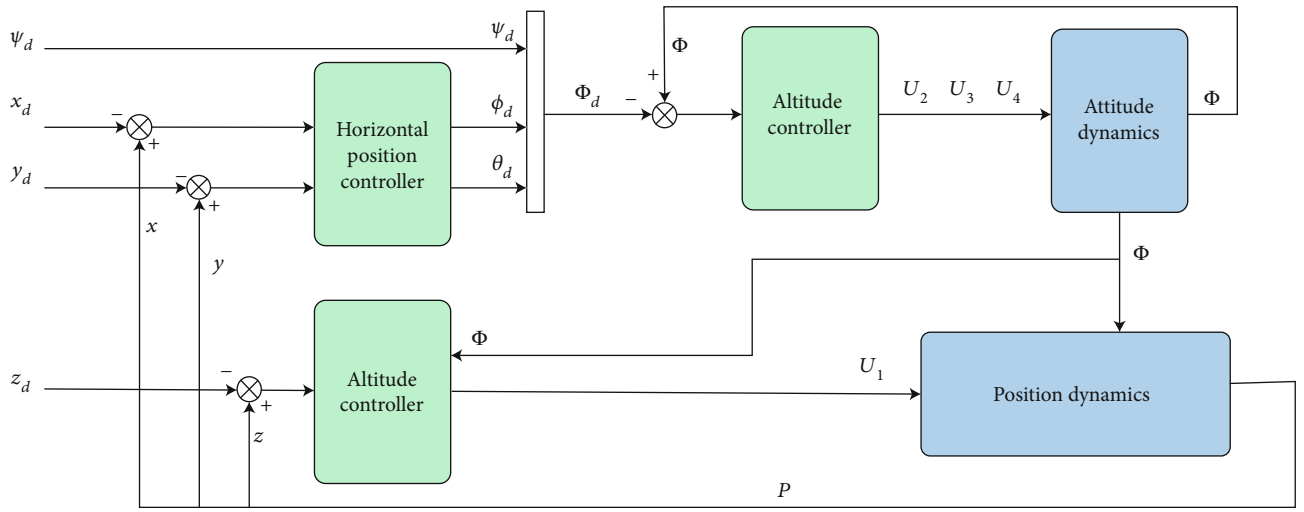

Figure 2: The UAV system control block diagram.

$$\ddot{\phi} = \frac{I_y - I_z}{I_x}\dot{\theta}\dot{\psi} + \frac{lU_2}{I_x} + D_\phi,$$
$$\ddot{\theta} = \frac{I_z - I_x}{I_y}\dot{\phi}\dot{\psi} + \frac{lU_3}{I_y} + D_\theta, \quad (2)$$
$$\ddot{\psi} = \frac{I_x - I_y}{I_z}\dot{\phi}\dot{\theta} + \frac{lU_4}{I_z} + D_\psi.$$

m is the mass of the system; g is the acceleration of gravity 9.8 m/s^2; $I = \text{diag}\{I_x, I_y, I_z\}$ is the moment of inertia corresponding; l is the distance from the centre of the body to the motor shaft; k_t is the drag coefficient; $D_i(i = x, y, z, \phi, \theta, \psi)$ represents external disturbances for each channel; U_1 is the total lift of the UAV system; and U_2, U_3, U_4 are the torque on each axis. The control block diagram of the UAV system is shown in Figure 2.

While the pitch angle changes, we can know from equation (1) that a force will be generated along the x-axis direction of the system. Therefore, when the aerial manipulator system is in contact with the environment at a certain pitch angle, there will be generated an acting force F and a reaction force $-F$ between the body and the environment, and the pair of acting forces is always perpendicular to the contacted surface. Hence, the dynamic relationship between the system attitude and the contact force when the contact reaches the steady state is as follows:

$$U_1\left(C_\phi S_\theta C_\psi + S_\phi S_\psi\right) = F,$$
$$U_1\left(C_\phi S_\theta S_\psi - S_\phi S_\psi\right) = 0, \quad (3)$$
$$U_1 C_\phi C_\theta = mg.$$

Set the yaw angle ψ to zero, and the contact force F expression can be expressed as follows:

$$F = mg\tan\theta, \quad (4)$$

$$\theta_d = \arctan\left(\frac{F_d}{mg}\right). \quad (5)$$

F_d represents the expected contact force, and θ_d is the corresponding pitch angle.

As shown in Figure 3, when the system is in the stable contact state, the gravity and pitch angle determine the contact force so that the force value can be obtained from equation (4). Therefore, the corresponding pitch angle is desired when the contact force reaches the desired value. Thus, we obtain the desired pitch by equation (5) and regard it as the system tracking object to implement the desired force indirectly. The control block diagram of the aerial manipulator is shown in Figure 4.

3. Controller Design

Stable flight is essential prior to performing the contact task. So, the system should hold stability with disturbance influence firstly. The UAV control system consists of two systems, an outer loop system controlling the position and an inner loop system controlling the attitude. In this section, a composite controller based on the extended state observer (ESO) and nonsingular global fast terminal sliding mode algorithm is designed for each subsystem to achieve the purpose of flight.

3.1. Extended State Observer Design

3.1.1. Extended State Observer of Position System. The decoupling design of the controller for the observer to accurately estimate the interference $D_i(i = x, y, z)$ is realized by introducing three virtual control variables u_x, u_y, u_z into the position system.

$$u_x = \frac{U_1}{m}\left(C_\phi S_\theta C_\psi + S_\phi S_\psi\right),$$
$$u_y = \frac{U_1}{m}\left(C_\phi S_\theta S_\psi - S_\phi C_\psi\right), \quad (6)$$
$$u_z = \frac{U_1}{m} C_\phi C_\theta.$$

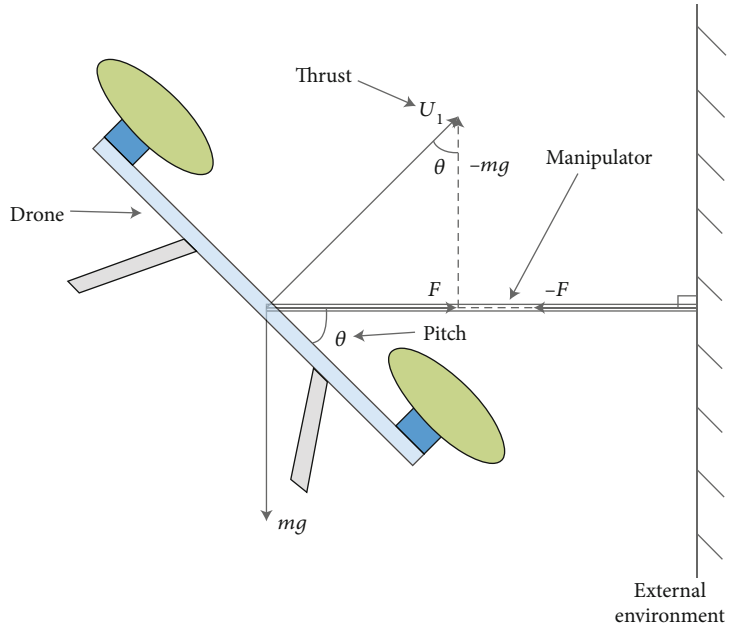

Figure 3: The dynamic relationship of the contact force of the aerial manipulator.

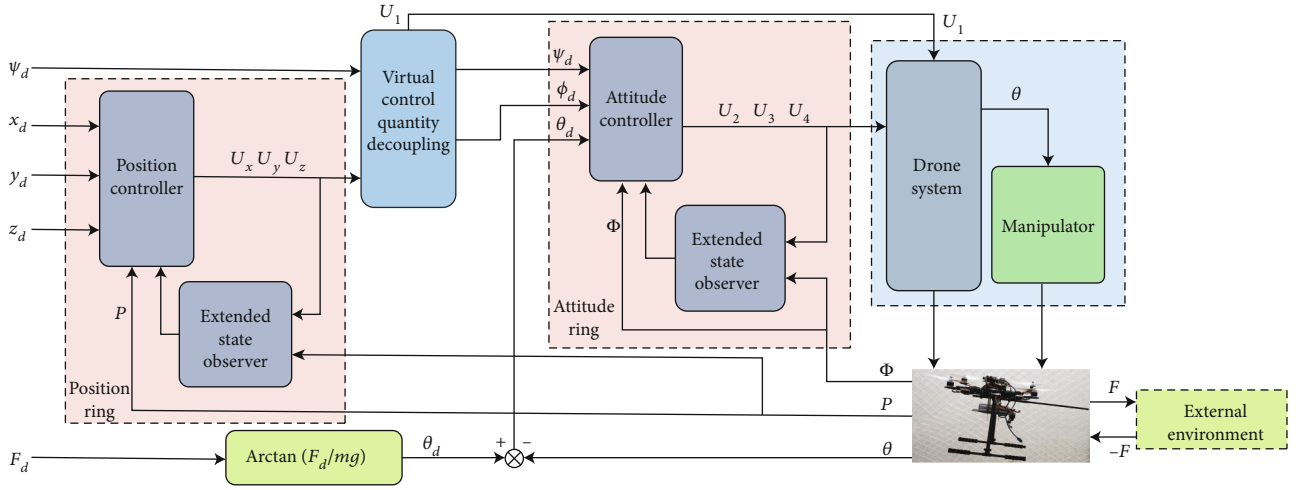

Figure 4: Contact force control of the aerial manipulator.

Defining the position errors of x, y, z, we can obtain the dynamic tracking errors of the position from equations (1) and (6).

$$e_x = x - x_d,\ e_y = y - y_d,\ e_z = z - z_d, \tag{7}$$

$$\begin{aligned} \ddot{e}_x &= u_x - \frac{k_t \dot{x}}{m} + \frac{D_x}{m} - \ddot{x}_d, \\ \ddot{e}_y &= u_y - \frac{k_t \dot{y}}{m} + \frac{D_y}{m} - \ddot{y}_d, \\ \ddot{e}_z &= u_z - \frac{k_t \dot{z}}{m} + \frac{D_z}{m} - \ddot{z}_d. \end{aligned} \tag{8}$$

Assuming that the disturbance is bounded and satisfies $\lim_{t \longrightarrow \infty} \dot{D}_{\mathrm{i}} = 0$, then the position system extended state observer is designed as

$$\begin{aligned} \dot{z}_{\mathrm{i}1} &= u_{\mathrm{i}} - \frac{k_t \dot{\mathrm{i}}}{m} + z_{\mathrm{i}2} + \eta_1 (z_{\mathrm{i}1} - \dot{e}_{\mathrm{i}}), \\ \dot{z}_{\mathrm{i}2} &= \eta_2 (z_{\mathrm{i}1} - \dot{e}_{\mathrm{i}}), \\ z_{\mathrm{i}2} &= \frac{\widehat{D}_{\mathrm{i}}}{m}. \end{aligned} \tag{9}$$

η_1 , η_2 are negative constants and the extended state observer gains. $\widehat{D}_i (i = x, y, z)$ is the estimated value of the external disturbance $D_i (i = x, y, z)$.

3.1.2. Extended State Observer of Attitude System. Considering the superior performance of the extended state observer in the decoupling control of multivariable systems [26], we regard the cross-coupling terms $((I_y - I_z)/I_x)\dot{\theta}\dot{\psi}, ((I_z - I_x)/I_y)\dot{\phi}\dot{\psi}, ((I_x - I_y)/I_z)\dot{\phi}\dot{\theta}$ in the system model (2) as internal

disturbances. The internal disturbances, together with the external disturbances, are evaluated by the extended state observer.

$$\begin{aligned}\ddot{\phi} &= \frac{lU_2}{I_x} + L_\phi,\\ \ddot{\theta} &= \frac{lU_3}{I_y} + L_\theta,\\ \ddot{\psi} &= \frac{lU_4}{I_z} + L_\psi.\end{aligned} \tag{10}$$

$L_\phi = ((I_y - I_z)/I_x)\dot{\theta}\dot{\psi} + D\,\phi, L_\theta = ((I_z - I_x)/I_y)\dot{\phi}\dot{\psi} + D_\theta$, $L_\psi = ((I_x - I_y)/I_z)\dot{\phi}\dot{\theta} + D_\psi$ are the lumped disturbances of the attitude system. Defining the position errors of ϕ, θ, ψ, we can obtain the dynamic tracking errors of the attitude as follows:

$$\begin{aligned}e_\phi = \phi - \phi_d, e_\theta = \theta - \theta_d, e_\psi = \psi - \psi_d,\\ \ddot{e}_\phi = \frac{lU_2}{I_x} + L_\phi - \ddot{\phi}_d,\\ \ddot{e}_\theta = \frac{lU_3}{I_y} + L_\theta - \ddot{\theta}_d,\\ \ddot{e}_\psi = \frac{lU_4}{I_z} + L_\psi - \ddot{\psi}_d.\end{aligned} \tag{11}$$

Assuming that the disturbance $L_i(i = \phi, \theta, \psi)$ is bounded and satisfies $\lim_{t\longrightarrow\infty} \dot{L}_i = 0$, then the attitude system extended state observer is designed as follows:

$$\begin{aligned}\dot{v}_{i1} &= \ddot{e}_i + \eta_3(v_{i1} - \dot{e}_i),\\ \dot{v}_{i2} &= \eta_4(v_{i1} - \dot{e}_i),\\ v_{i2} &= \widehat{L}_i.\end{aligned} \tag{12}$$

η_3 , η_4 are negative constants and the extended state observer gains, respectively. $\widehat{L}_i(i = \phi, \theta, \psi)$ is the estimated value of the external disturbance.

3.1.3. Convergence Judgment. Since the design form of the extended state observer for the position system is the same, the x channel is taken as an example to prove the convergence, and the same is true for the y and z channels. The ESO error of the x channel is defined and combined with equation (8) to obtain the following [27]:

$$\begin{aligned}e_{x1} &= z_{x1} - \dot{x},\\ e_{x2} &= z_{x2} - F_{dx},\end{aligned} \tag{13}$$

$$\begin{bmatrix}\dot{e}_{x1}\\ \dot{e}_{x2}\end{bmatrix} = \begin{bmatrix}\eta_1 & 1\\ \eta_2 & 0\end{bmatrix} \bullet \begin{bmatrix}e_{x1}\\ e_{x2}\end{bmatrix} + \begin{bmatrix}0\\ -\dfrac{\dot{D}_x}{m}\end{bmatrix}. \tag{14}$$

For a linear system $\dot{x} = Ax + Bx$, if the matrix A satisfies the Hurwitz matrix that the real part of each eigenvalue is less than zero, and u is bounded to meet $\lim_{t\longrightarrow\infty} u = 0$, then the system is asymptotically stable [28]. We can obtain that the real part of the eigenvalues of the matrix

$$\begin{bmatrix}\eta_1 & 1\\ \eta_2 & 0\end{bmatrix} \tag{15}$$

is $\lambda_1 = \lambda_2 = \eta_1/2$. Since η_1 is a negative constant, the matrix satisfies the Hurwitz matrix. In addition, D_x is bounded and satisfies $\lim_{t\longrightarrow\infty} \dot{D}_x = 0$ based on the assumption. Therefore, we know that system (14) is asymptotically stable. That is, the error of the extended state observer meets $\lim_{t\longrightarrow\infty} e_{x1} = 0$, $\lim_{t\longrightarrow\infty} e_{x2} = 0$, and the external disturbance estimate $\widehat{D}_x$ satisfies $\lim_{t\longrightarrow 0} \widehat{D}_x = D_x$. Similarly, we can prove that the y- and z-channel interference estimate values $\widehat{D}_y, \widehat{D}_z$ can asymptotically converge to the actual values D_y, D_z. Since the ESO design form of the attitude system is the same as that of the position system, the above convergence can be generalized to the attitude system.

3.2. Composite Controller Design. Since the aerial manipulator system is strongly coupled and underactuated, it is impossible to simultaneously track all degrees of freedom.

3.2.1. Height Controller Design. The nonsingular global fast terminal sliding mode function is designed as follows:

$$s = \dot{e} + \alpha e^k + \frac{1}{\beta}|e|^{p/q}\ \mathrm{sgn}\,(e). \tag{16}$$

Defining the dynamic error as equation (8), the composite nonsingular global fast terminal sliding mode controller for the z channel is designed as follows:

$$\begin{aligned}u_z = \frac{k_t\dot{z}}{m} + g - \left[\frac{\widehat{D}_z}{m} + \gamma s + \lambda sgn\left(\frac{s}{\varepsilon}\right) + \alpha k e^{k-1}\dot{e}_z\right.\\ \left. + \frac{1}{\beta}\frac{p}{q}|e_z|^{p/q-1}\dot{e}_z\ \mathrm{sgn}\,(e)\right],\\ U_1 = \frac{mu_z}{C_\phi C_\theta}.\end{aligned} \tag{17}$$

z d is the desired height; $\alpha > 0, \beta > 0, k > 0, p/q > 0$; $\gamma > 0, \lambda > 0, \varepsilon > 0$; p, q are all positive odd numbers; and sgn (e) is the switching function about the error.

3.2.2. Horizontal Position Controller Design. Horizontal position controllers of the x and y channels are designed to obtain the desired pitch and roll angles. We can obtain from equation (6) the following:

$$\sin\theta_d = \frac{mu_x}{U_1\cos\theta_d\cos\psi_d} - \frac{\sin\phi_d\sin\psi_d}{\cos\phi_d\cos\psi_d}, \tag{18}$$

$$\sin\phi_d = m\frac{u_x\sin\psi_d - u_y\cos\psi_d}{U_1}. \tag{19}$$

Define the desired position of the system in the horizontal plane as (x_d, y_d). Hence, the horizontal position errors are $e_x = x - x_d$ and $e_y = y - y_d$. Setting the yaw angle $\psi_d = 0$, equations (18) and (19) can be simplified as follows:

$$\sin\theta_d = \frac{mu_x}{U_1 \cos\phi_d}, \tag{20}$$

$$\sin\phi_d = -\frac{mu_y}{U_1}. \tag{21}$$

Hence, the horizontal position controllers are designed as follows:

$$\begin{aligned} u_x &= \frac{k_t\dot{x}}{m} - \left[\frac{\hat{D}_x}{m} + \gamma s + \lambda sgn\left(\frac{s_x}{\varepsilon}\right) + \alpha k e^{k-1}\dot{e}_x + \frac{1}{\beta}\frac{p}{q}\dot{e}_x|e_x|^{p/q-1}\ \text{sgn}\ (e_x)\right], \\ u_y &= \frac{k_t\dot{y}}{m} - \left[\frac{\hat{D}_y}{m} + \gamma s + \lambda sgn\left(\frac{s_y}{\varepsilon}\right) + \alpha k e^{k-1}\dot{e}_y + \frac{1}{\beta}\frac{p}{q}\dot{e}_y|e_y|^{p/q-1}\ \text{sgn}\ (e_y)\right]. \end{aligned} \tag{22}$$

To avoid the inability to solve when the right side of the above equation exceeds $[-1, 1]$, we define $X = mu_x/U_1 \cos\phi_d$, $Y = -(mu_y/U_1)$.

$$\begin{aligned} \theta_d &= -\frac{\pi}{2}, && X<-1, \\ \theta_d &= \arctan X, && -1 \le |X| \le 1, \\ \theta_d &= \frac{\pi}{2}, && X > 1, \\ \phi_d &= -\frac{\pi}{2}, && Y<-1, \\ \phi_d &= \arctan Y, && -1 \le |Y| \le 1, \\ \phi_d &= \frac{\pi}{2}, && Y > 1. \end{aligned} \tag{23}$$

3.2.3. Attitude Controller Design. Since we obtain the desired pitch angle and roll angle from equations (5) and (21), the attitude tracking errors are defined as the following equation.

$$\begin{aligned} e_\phi &= \phi - \phi_d, \\ e_\theta &= \theta - \theta_d, \\ e_\psi &= \psi - \psi_d. \end{aligned} \tag{24}$$

To avoid the attitude system's dynamic performance affecting the position system's stability, the attitude controller's gains are adjusted to ensure that the attitude error convergence is faster than that of the position errors. Hence, the attitude controllers are designed as follows:

$$\begin{aligned} U_2 &= -\left[\hat{D}_\phi + \gamma s + \lambda sgn\left(\frac{s_\phi}{\varepsilon}\right) + \alpha k e_\phi^{k-1}\dot{e}_\phi + \frac{1}{\beta}\frac{p}{q}|e_\phi|^{p/q-1}\dot{e}_\phi\ \text{sgn}\ (e_\phi)\right]\frac{I_x}{l}, \\ U_3 &= -\left[\hat{D}_\theta + \gamma s + \lambda sgn\left(\frac{s_\theta}{\varepsilon}\right) + \alpha k e_\theta^{k-1}\dot{e}_\theta + \frac{1}{\beta}\frac{p}{q}|e_\theta|^{p/q-1}\dot{e}_\theta\ \text{sgn}\ (e_\theta)\right]\frac{I_y}{l}, \\ U_4 &= -\left[\hat{D}_\psi + \gamma s + \lambda sgn\left(\frac{s_\psi}{\varepsilon}\right) + \alpha k e_\psi^{k-1}\dot{e}_\psi + \frac{1}{\beta}\frac{p}{q}|e_\psi|^{p/q-1}\dot{e}_\psi\ \text{sgn}\ (e_\psi)\right]I_z. \end{aligned} \tag{25}$$

$\alpha > 0, \beta > 0, k > 0, \gamma > 0, \lambda > 0, \varepsilon > 0, p/q > 0$; p, q are positive odd numbers; and sgn (s) is a switching function on the error.

3.2.4. Controller Convergence Judgement. Since the position controllers have the same design form, the z-channel controller is regarded as an example to prove the convergence. The convergence is also suitable for the x- and y-channel controllers. The Lyapunov function is defined as follows:

$$\begin{aligned} V &= V_a + V_s, \\ V_a &= \frac{1}{2}s^2, \\ V_s &= \frac{1}{2}e^2. \end{aligned} \tag{26}$$

V_a represents the process of the system approaching the sliding surface; V_s represents the process after the system state reaches the sliding surface. When the system reaches the sliding mode surface $s = 0$, we can obtain $\dot{V}_a$, $\dot{V}_s$ as follows:

$$\begin{aligned} \dot{V}_a &= s\dot{s} = -\left(\gamma s^2 + \lambda\frac{|s|}{\varepsilon}\right), \\ \dot{V}_s &= e\dot{e} = -\left(\alpha e^{k+1} + \frac{1}{\beta}|e|^{p/q+1}\right). \end{aligned} \tag{27}$$

Since $\alpha, \beta, \lambda, \gamma$ are positive numbers, $V > 0, V \cdot \dot{V} \le 0$. According to the Lyapunov stability criterion, the system is asymptotically stable, so the error can gradually converge to zero from any initial value.

Since the position and attitude systems have the same design form on the composite controllers, the convergence of the attitude controller can be an expansion that can be obtained from the proof mentioned above. Hence, the attitude controller (25) can be guaranteed to converge the attitude error to zero within a finite time.

3.3. Performance Comparison. To evaluate the controller's performance when the aerial manipulator is in contact with the environment, the system contact will be simulated in the next section by Simulink. As shown in Figure 5, we developed an aerial manipulator system consisting mainly of the aircraft, the fixed manipulator, and the onboard computer. The flight controller is the open-source flight control Pixhawk [29], and the onboard computer is Raspberry Pi4b. The physical parameters of the system are shown in Table 1.

The simulation results obtained by the proposed controller (Composite Nonsingular Global Fast Terminal Sliding

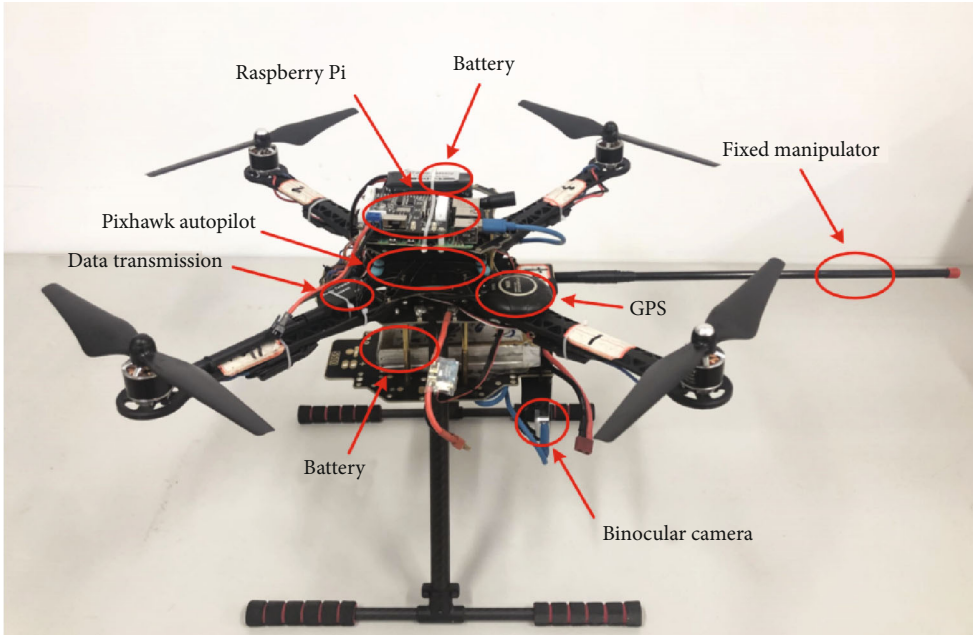

Figure 5: The aerial manipulator system.

Table 1: Parameters of the aerial manipulator system.

Parameter	Value	Parameter	Value
System mass	1.8 kg	$I_x(\text{kg•m}^{-2})$	0.1535
Paddle distance	9.4 × 4.3 inch	$I_y(\text{kg•m}^{-2})$	0.1535
Wheelbase	500 mm	$I_z(\text{kg•m}^{-2})$	0.3070
Arm length	500 mm	$g(\text{m•s}^{-2})$	9.8

Table 2: Parameters of the position system controller.

Parameter	Value	Parameter	Value	Parameter	Value
λ	10	β	50	q	3
γ	2	k	1	ε	2
α	20	p	5	k_t	0.09

Mode, CNGFTSM) and the other four controllers under the same conditions are compared to analyze the results: Nonsingular Global Fast Terminal Sliding Mode controller (GFTSM), Composite Nonsingular Sliding Mode controller (CNSM) combined with extended state observer and nonsingular sliding mode algorithm, composite PID controller combined with extended state observer and PID algorithm (CPID), and Integral Backstepping Control (IBC) [30]. In order to simulate the external wind disturbance during the flight, set the wind disturbance as a combination of fundamental wind and gradual wind. The fundamental wind is a constant that does not change with time, and the gradual wind changes regularly. The specific settings are the following equations.

Table 3: Parameters of the attitude system controller.

Parameter	Value	Parameter	Value	Parameter	Value
λ	20	β	200	q	3
γ	80	k	1	ε	2
α	100	p	3		

Table 4: Parameters of the extended state observer.

Parameter	Value	Parameter	Value
η_{i1}	-20	η_{i3}	-60
η_{i2}	-400	η_{i4}	-900

Table 5: The effect of design parameters on control performance.

Parameter	Effect on control performance
$\gamma, \lambda, \varepsilon$	γ determines the system's speed approaching the sliding mode when large step responses. λ, ε determine the speed at which the system is about to reach the sliding mode.
α, β, p, q, k	In the sliding mode, the nonlinear part parameters β, p, q determine the speed at which the system converges from the initial state to the stable state, and the farther away from the equilibrium state, the faster the convergence. α, k determine the system's speed about reaching a stable state. p, q are also exponential factors that determine the nonsingularity of the sliding mode.
η_i	$\eta_i$is a high-gain error feedback parameter, which makes the dynamics of the observer much higher than that of the system's, which is equivalent to a fast-changing subsystem in the system, thus ensuring that the observer error can converge quickly and have a sufficiently high estimation accuracy.

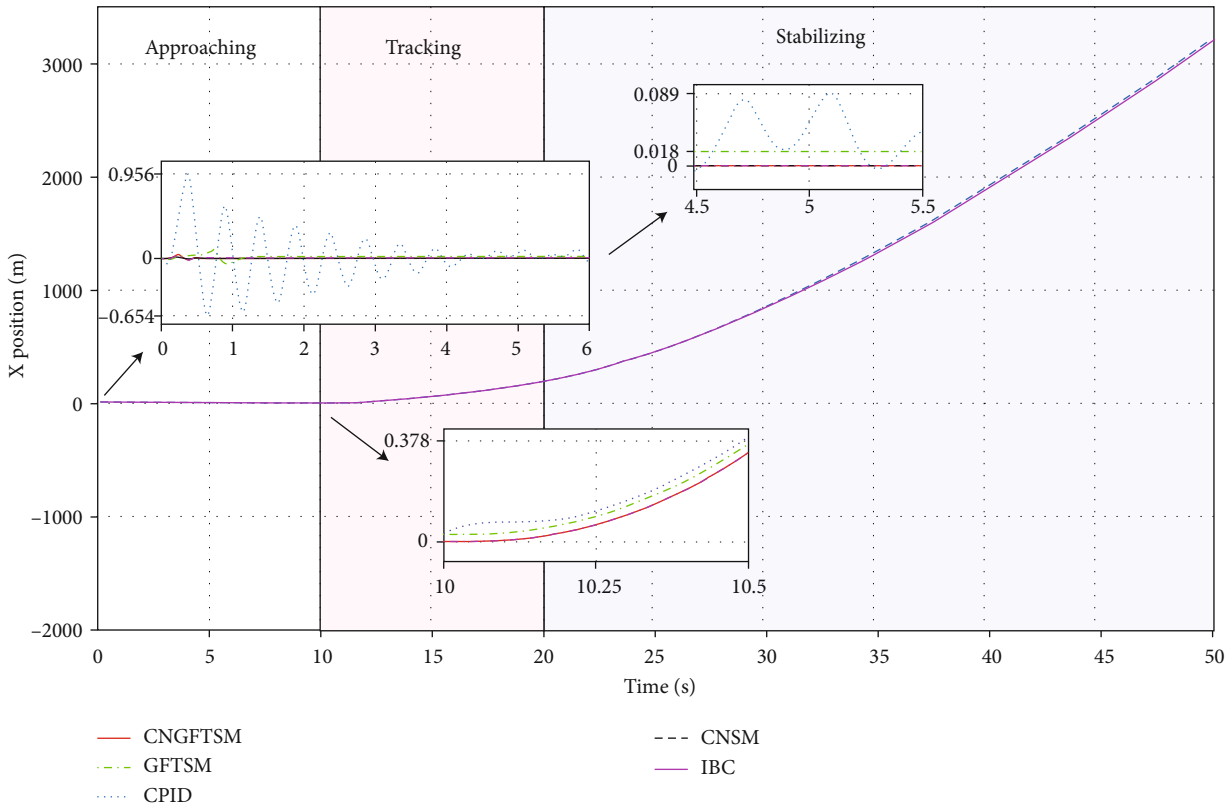

(a)

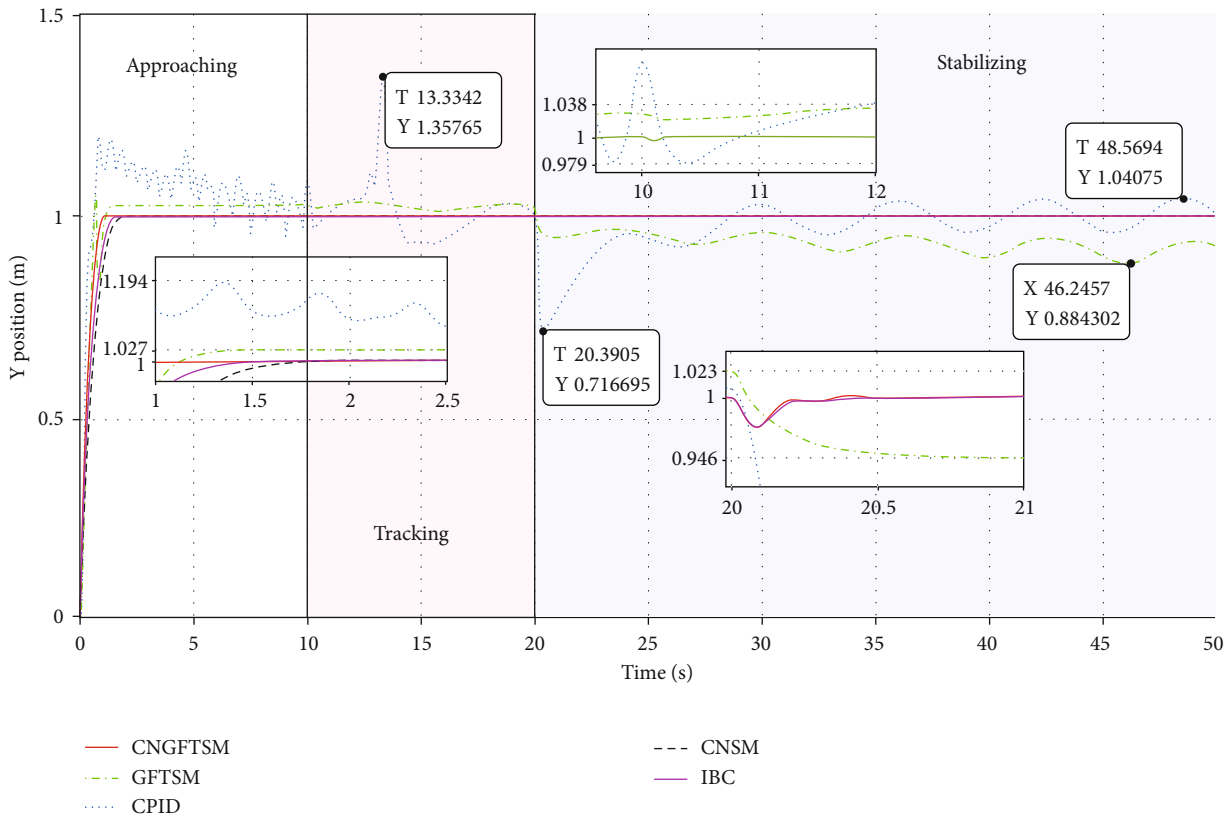

(b)

Figure 6: Continued.

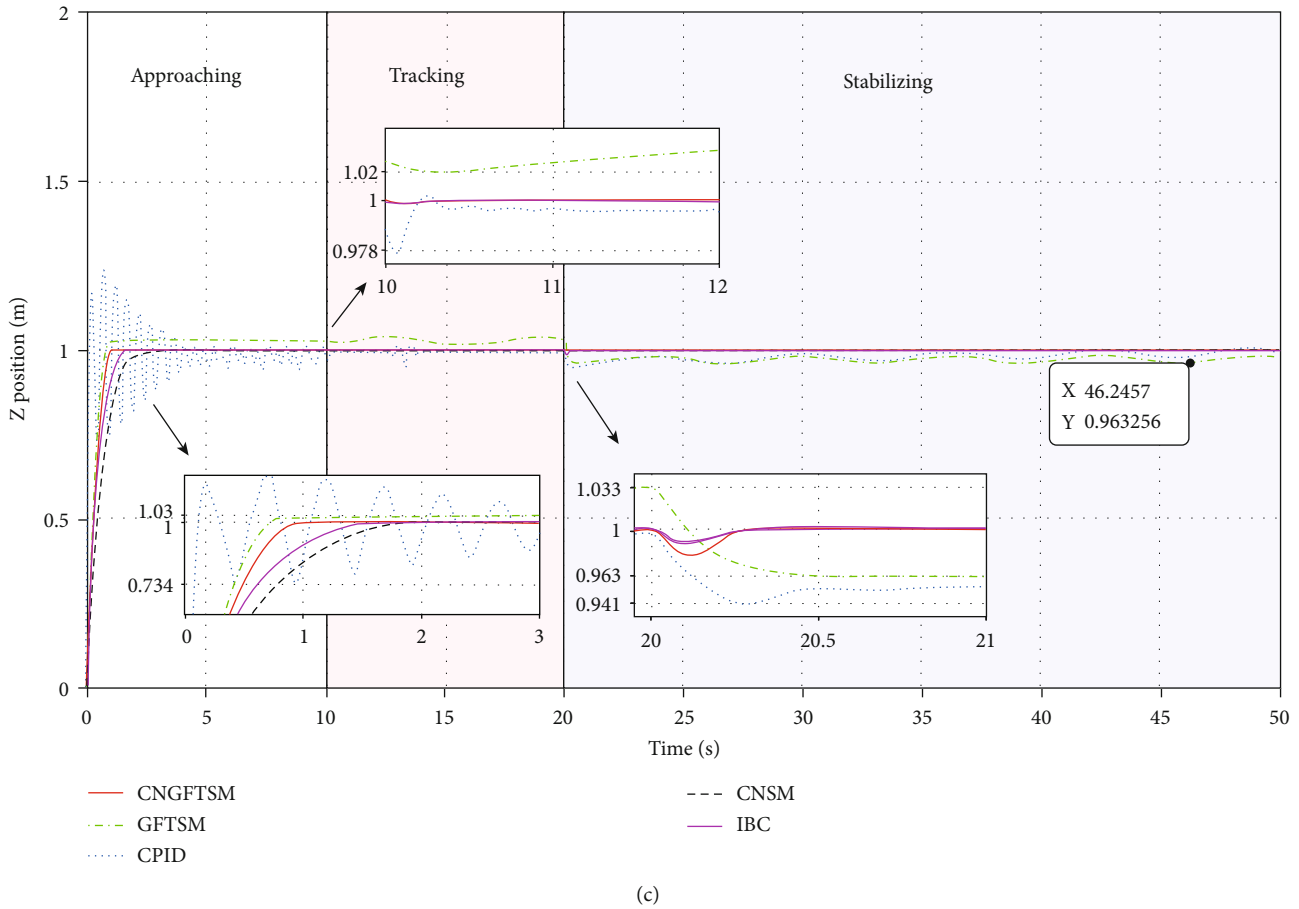

(c)

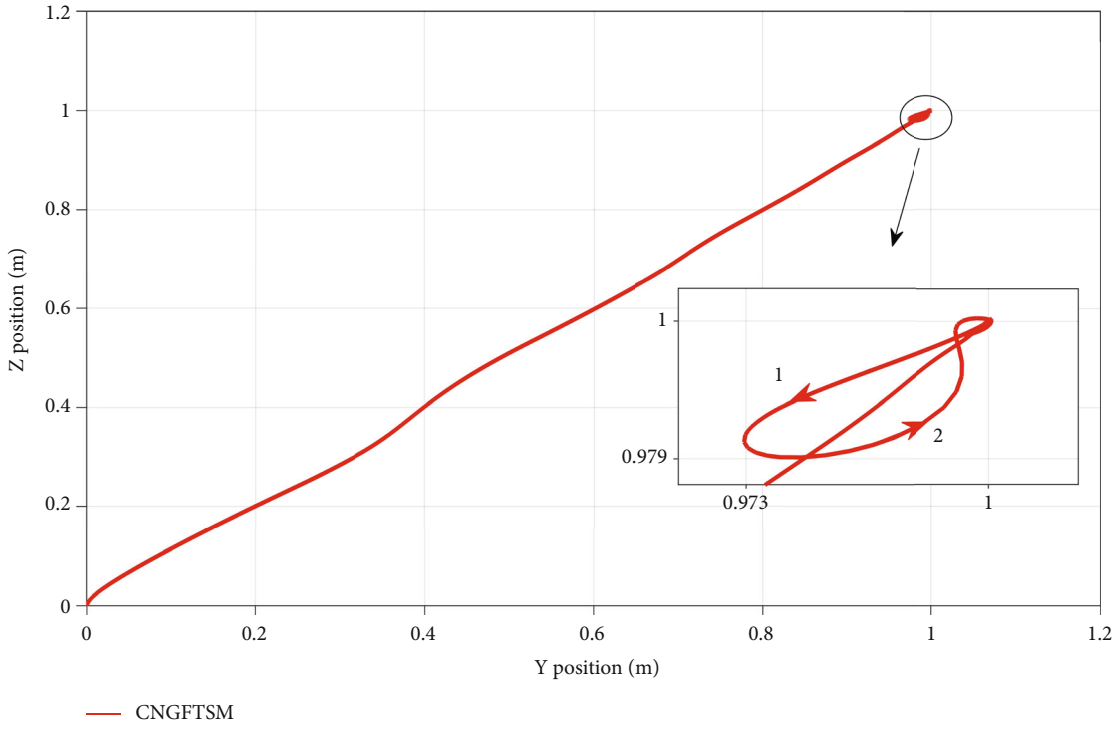

(d)

Figure 6: The position results of simulations. (a) Position changes in the x-axis direction. (b) Position changes in the y-axis direction. (c) Position changes in the z-axis direction. (d) Position changes in the y - z plane.

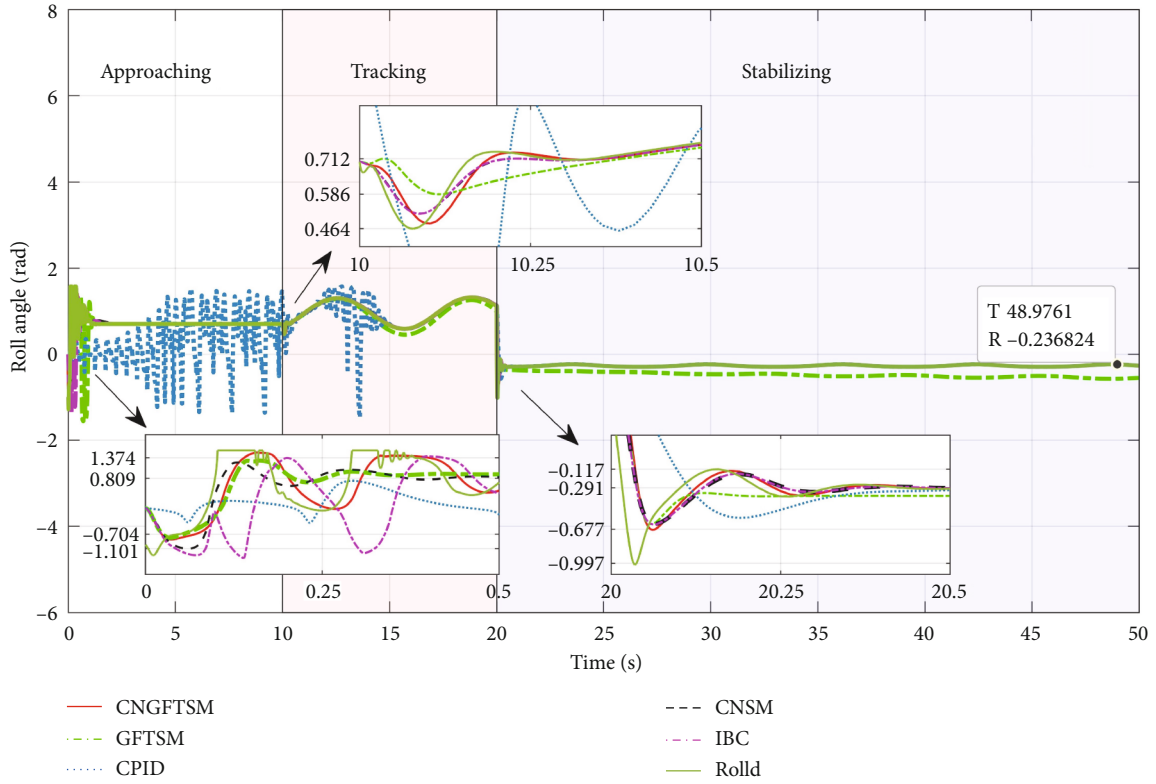

(a)

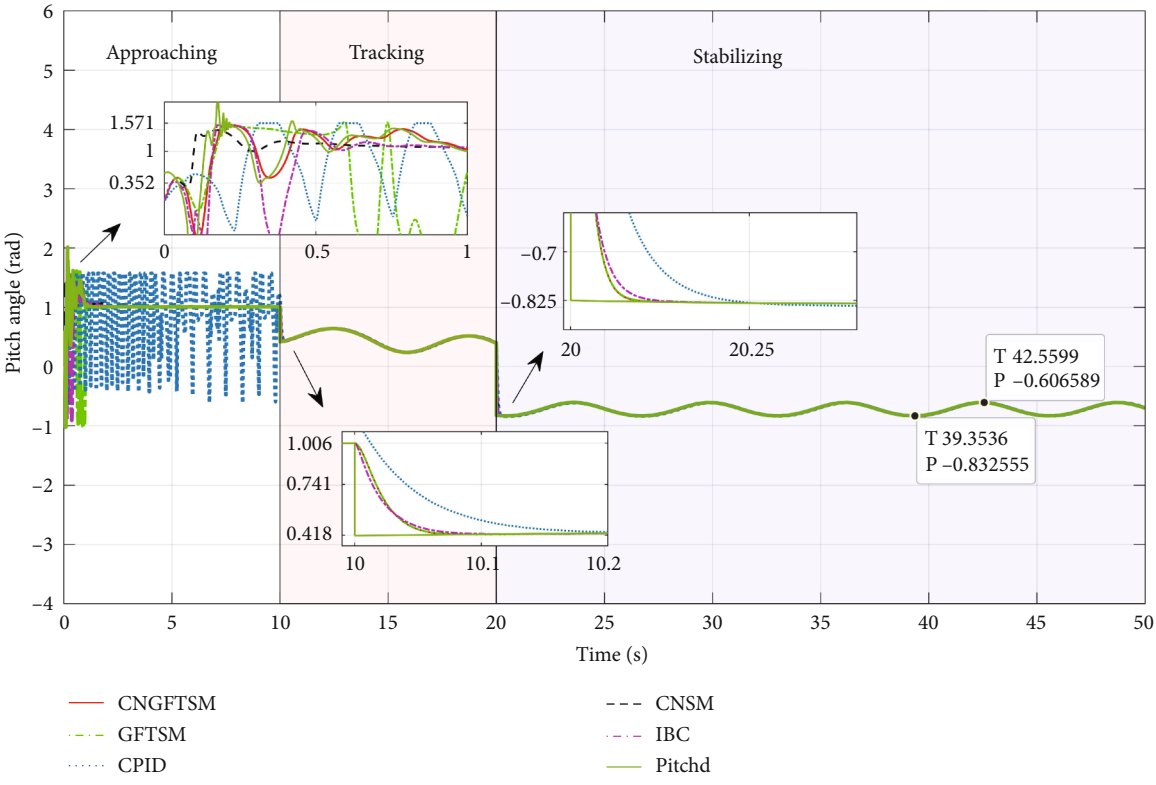

(b)

Figure 7: Continued.

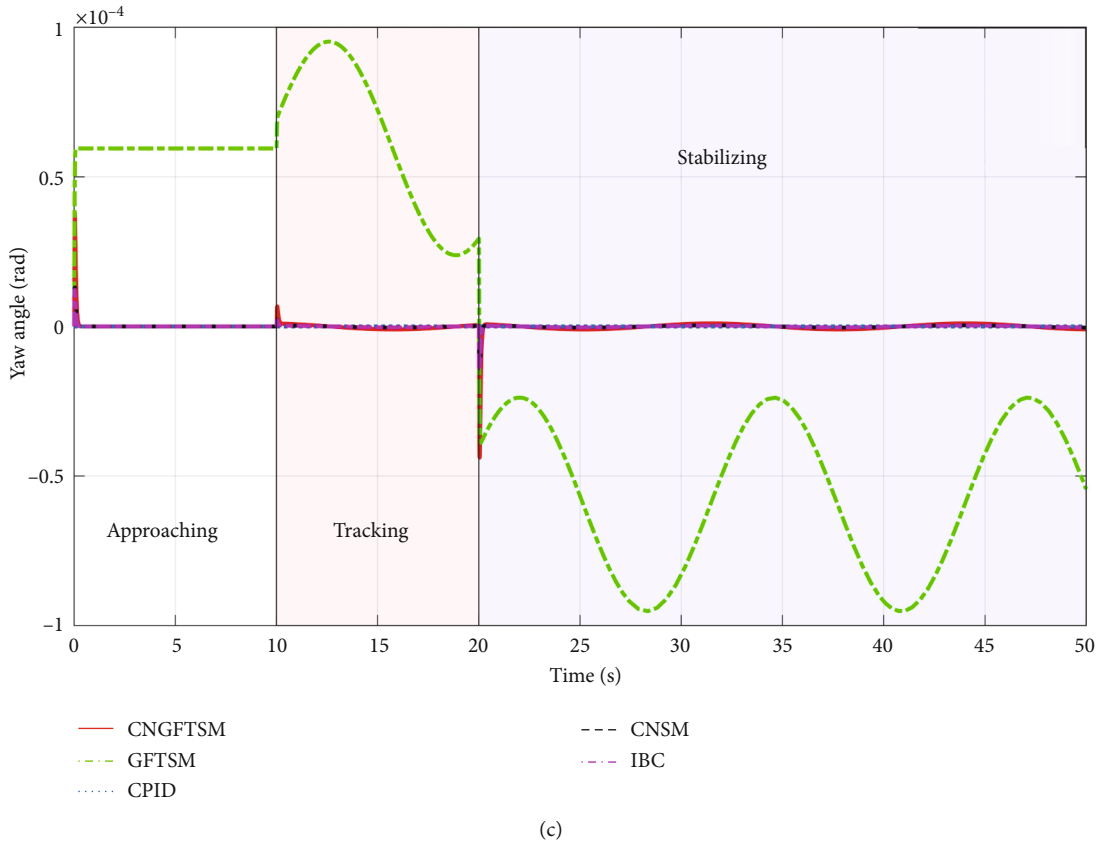

(c)

Figure 7: The attitude results of simulations. (a) Roll angle changes for disturbance rejection. (b) Pitch angle changes to track the desired contact force. (c) Yaw angle changes for disturbance rejection.

$$\frac{D_i}{m}(i=x,y,z)=\begin{cases}6, & t\le 10,\\ 6+2\cdot\cos(t), & 10<t\le 20,\\ -6-2\cdot\sin(t), & t>20,\end{cases} \tag{28}$$

$$D_i(i=\phi,\theta,\psi)=\begin{cases}0.5, & t\le 10,\\ 0.5+0.3\cdot\cos(0.5t), & 10<t\le 20,\\ -0.5-0.3\cdot\sin(0.5t), & t>20.\end{cases} \tag{29}$$

The simulation process has three stages: 0-10 s is the approach stage, 10-20 s is the tracking stage, and the stabilize stage is after 20 s. The system keeps hovering after taking off from $(0,0,0)$ to $(0,1,1)$. Then, the system tracks a contact force with the slope of 0.5 N/s and a final value of 5 N forward along the x-axis in the 10-20 s. Finally, when the contact force reaches the wanted value, the system needs to keep the force value and the position in the y-z plane unchanged. Since there is no contacted object in the simulation, the results of the system's displacement on the x-axis will continue to increase.

The simulation results are evaluated from two aspects [31]: (1) force track accuracy. F_d represents the expected value of the contact force; F represents the actual value of the contact force. When the contact force reaches $F = F_d \pm 5\%$, the force control accuracy meets the requirements. (2) Position control accuracy. $\|\varepsilon_{\mathrm{UAV}}\| = \|r^{\mathrm{ref}}_{\mathrm{UAV}} - r_{\mathrm{UAV}}\|$, $\rho_{\mathrm{UAV}} = \|\varepsilon_{\mathrm{UAV}}\|/L$. r_{UAV} represents the position of the system in the inertial coordinate system; $\varepsilon_{\mathrm{UAV}}$ represents the position error of the system; L represents the effective length of the robotic arm beyond the body. When the position accuracy reaches $\rho \le 0.1L$, the position control accuracy meets the requirements. The controller and observer parameters are in Tables 2–4, and the effect of design parameters on control performance is listed in Table 5.

4. Simulation Results and Analysis

In Figures 6(a)–6(c) are the position change curves of the system in the x, y, z directions under the five control methods, and d is the trajectory change curve of the system in the y-z plane.

Figure 7 shows the change curves of the system attitude under the five control methods. *Rolld* and *Pitchd* are the desired roll and pitch angles, respectively. The expected value of the yaw angle is zero.

In Figure 8(a) is the tracking curves of the system to the desired contact force, and b is the change curves of the system lift under the five control methods.

Figures 9(a) and 9(b) show the tracking effect of the designed extended state observer on disturbances, and due to the similarity of the design forms, the position and

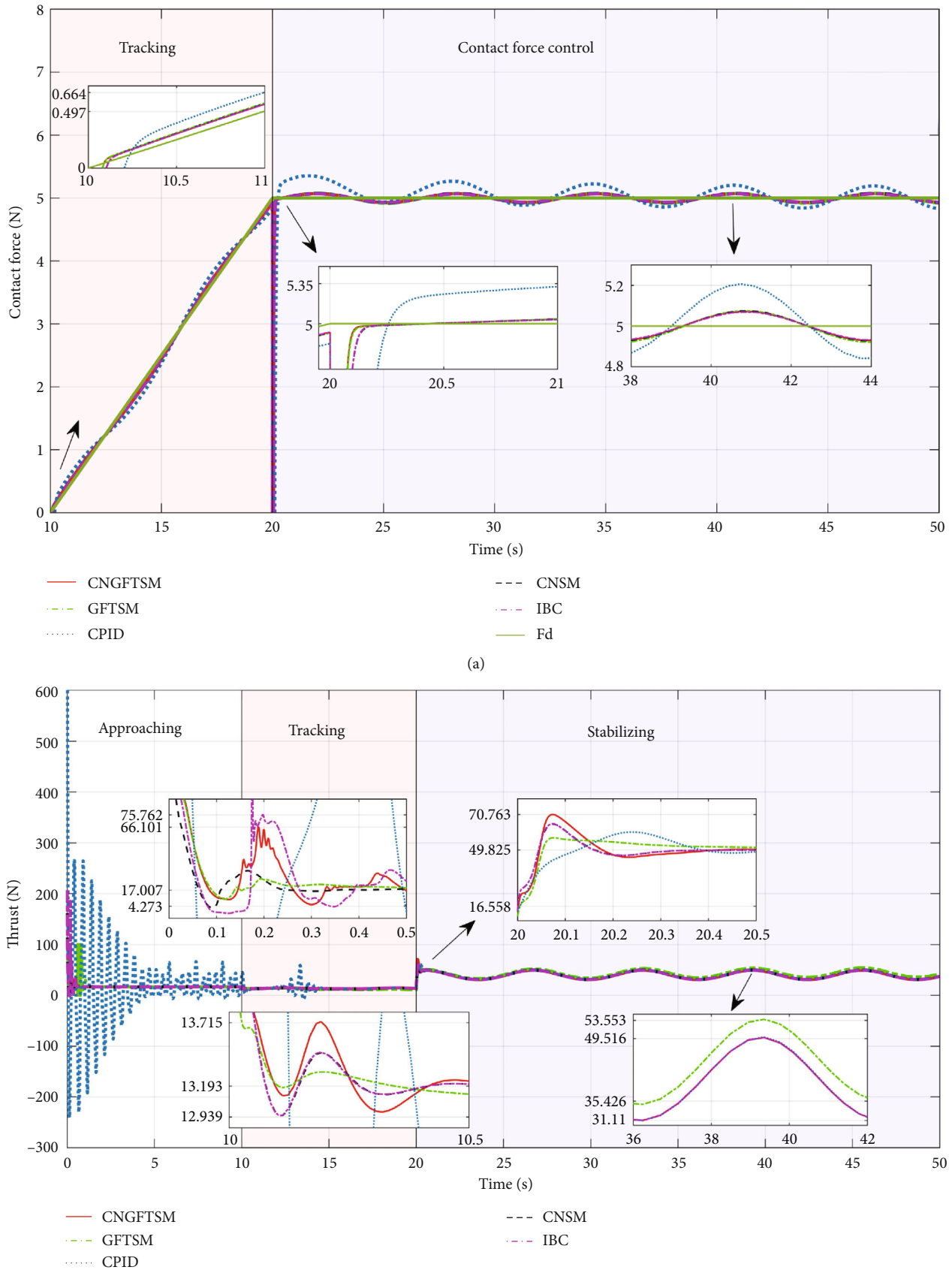

Figure 8: (a) The contact force between the system and the environment. (b) The system's thrust.

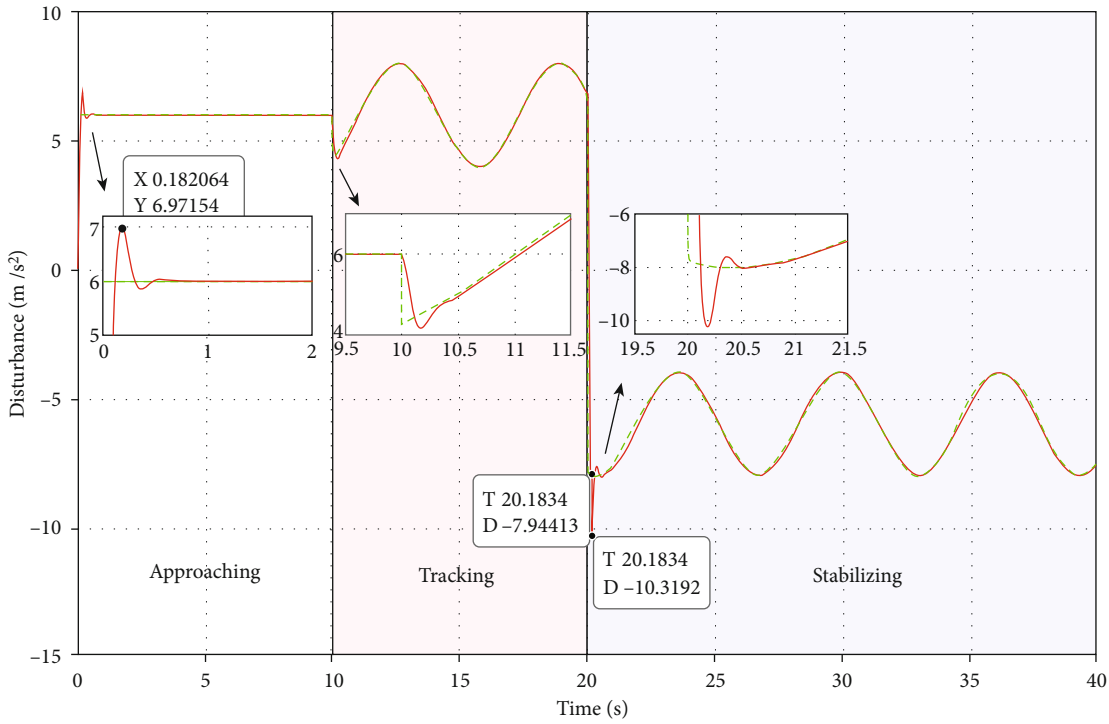

(a)

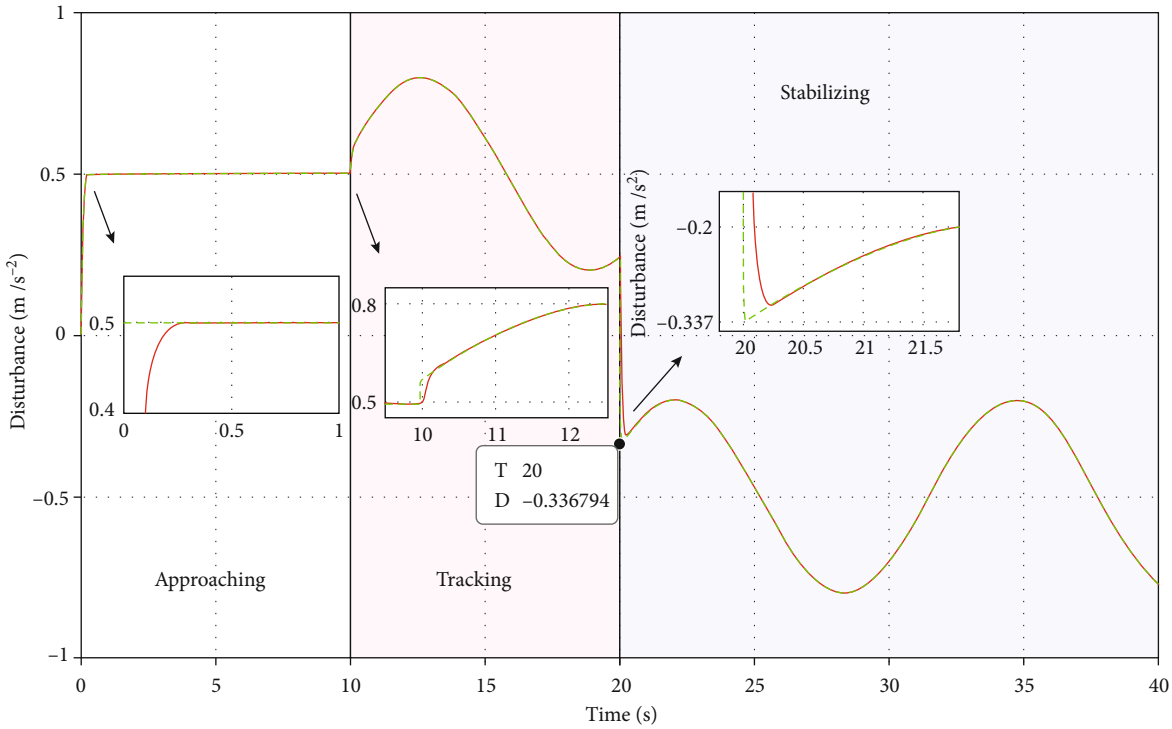

(b)

Figure 9: The disturbance estimation. (a) The estimation value of the z-channel. (b) The estimation value of the ϕ-channel.

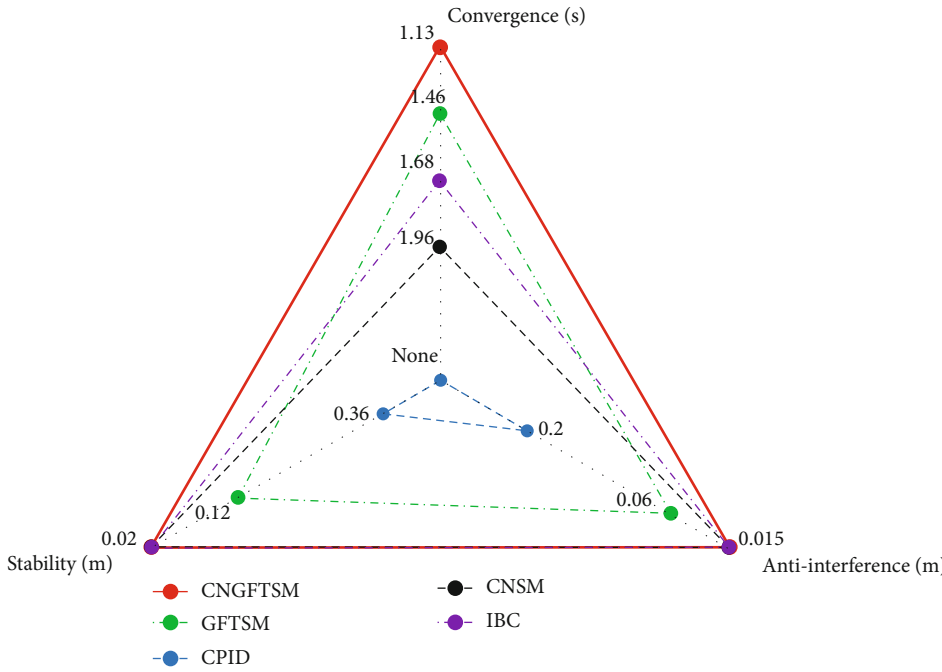

Figure 10: The comparison of five controllers. Numbers are calculated from simulation results and are inversely proportional to metrics; "none" means no convergence.

attitude systems are taken with the z channel and the ϕ channel as examples, respectively. $D_i\text{hat}(i = z, r)$ and $D_i(i = z, r)$ are the estimated and actual values, respectively.

4.1. Approaching Stage. The system moves from the starting position $(0, 0, 0)$ to $(0, 1, 1)$. As shown in Figure 6, the CNGFTSM controller converges the error the fastest, followed by the IBC and CNSM controllers. The CNGFTSM convergence is about 0.5 s less than that of the IBC and 1 s less than that of the CNSM. After reaching a stable state, the system using the GFTSM controller has errors of about 0.027 m and 0.03 m caused by the controller's inability to suppress disturbances actively on the y-axis and z-axis, and the CNGFTSM controller system has almost zero errors. As shown in Figure 7, in 0-10 seconds, the system needs to adjust the pitch angle to offset the acceleration caused by disturbances and guarantee system position zero in the x-axis direction. The roll and pitch angle curves of the CNGFTSM can closely follow the expected value changes, and the following and time errors do not exceed 0.1 rad and 0.1 s, respectively. The roll and pitch angle curves of the GFTSM, CNSM, and IBC controllers are more marked than those of the CNGFTSM controller. In addition, the lift curve of the GFTSM controller fluctuates wildly, CNGFTSM and IBC are relatively steady, and CNSM is the most stable. In contrast, the roll and pitch angles and lift curves of CPID appear to oscillate. However, the UAV motor is a mechanical device, and if its amplitude of speed changes too much, it will produce a lot of heat and violent vibration, eventually leading to mechanical failure. Therefore, the vibration of controller CPID is not conducive to the mechanical characteristics of UAV.

4.2. Tracking Stage. The system tracks the expected force along the x-axis after 10 s. Due to the disturbance changes from the essential wind to the asymptotic wind, the system needs to change the attitude and lift as the disturbance to ensure the position is unchanged in the y-z plane. From Figure 6, in the tracking phase, the position of the system using the CNGFTSM, CNSM, and IBC controllers changes much less than 0.01 m on the y- and z-axes. In contrast, the position error of the GFTSM controller is more than 0.02 m on the z-axis, and the CPID controller cannot converge the position errors. Since the manipulator effective length in this paper is $L = 0.2$ m, the position/control accuracy cannot meet the evaluation criteria because the position error exceeds 10% of L. In Figure 7, the roll and pitch angles of CNGFTSM, CNSM, CPID, and IBC controllers can accurately follow the alternation of the expected value within 0.1 s. The CPID controller cannot converge the roll angle because of the disturbance constantly changing. In Figure 8(a), the system using the CNGFTSM and GFTSM controllers reaches the desired contact force value the fastest, followed by those using the CNSM and IBC controllers. Moreover, the contact force errors are within 5% of the expected value, meeting the evaluation criteria. In Figure 9, the estimation of the extended state observer during the tracking phase is almost consistent with the disturbances, showing an excellent tracking ability.

4.3. Stable Stage. The aerial manipulator system should ensure that the force and position are unchanged in the stability control stage. In Figure 6, since the disturbance suddenly changes at 20 s, the system produces a small position error on the y- and z-axes and quickly converges to zero.

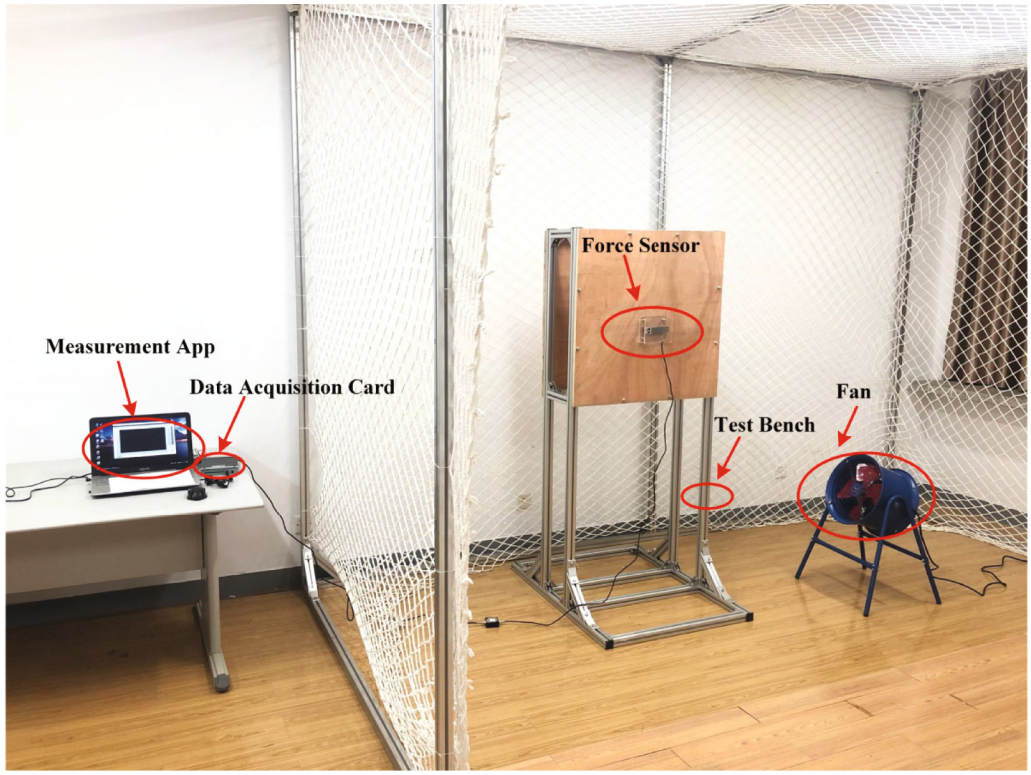

(a)

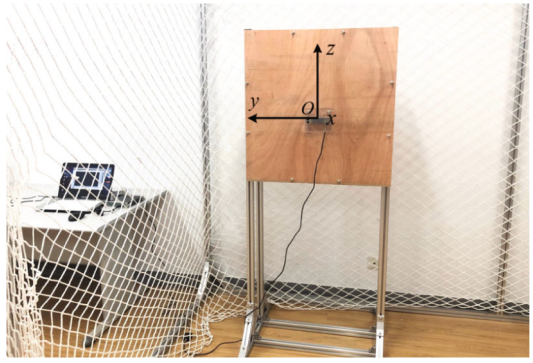

(b)

Figure 11: (a) The contact force measurement system. (b) The inertial coordinate system.

In Figure 6(b), the position errors of the CNGFTSM, CNSM, and IBC controllers are almost zero. The position error of the GFTSM controller is 0.023 m at 20 s and reaches 0.116 m at 46.24 s, and the CPID controller generates error varying with disturbances. This result indicates that the GFTSM and CPID controllers cannot guarantee the convergence of the system position on the y-axis. In Figure 8(a), due to the extended state observer's tracking delay of the actual interference value, the CNGFTSM contact force value changes regularly around the expected value with the maximum error of 0.074 N being unable to reach the desired value. If the disturbance is a constant, the actual contact force value will stably converge to the expected value. In Figure 9, the error and the delay of the extended state observer between the estimated value and the actual disturbance in the stabilizing stage are less than 0.1 m/s^2 and 0.2 s, respectively, indicating excellent estimation performance.

As shown in Figure 10, based on the simulation results of each controller, we use three metrics to evaluate the performance of the five controllers, taking the system position y as an example: (1) convergence—the time of the system to converge from the initial state to the desired state; (2) anti-interference—during the approaching, tracking, and stabilizing stages, the mean value of the maximum error from the expected value; (3) stability—during the three stages, the max oscillation amplitude of the curve.

In summary, the performance of the CNGFTSM controller is the best, followed by that of IBC and CNSM. In contrast, the GFTSM controller can only ensure contact force convergence, and the CPID controller can guarantee

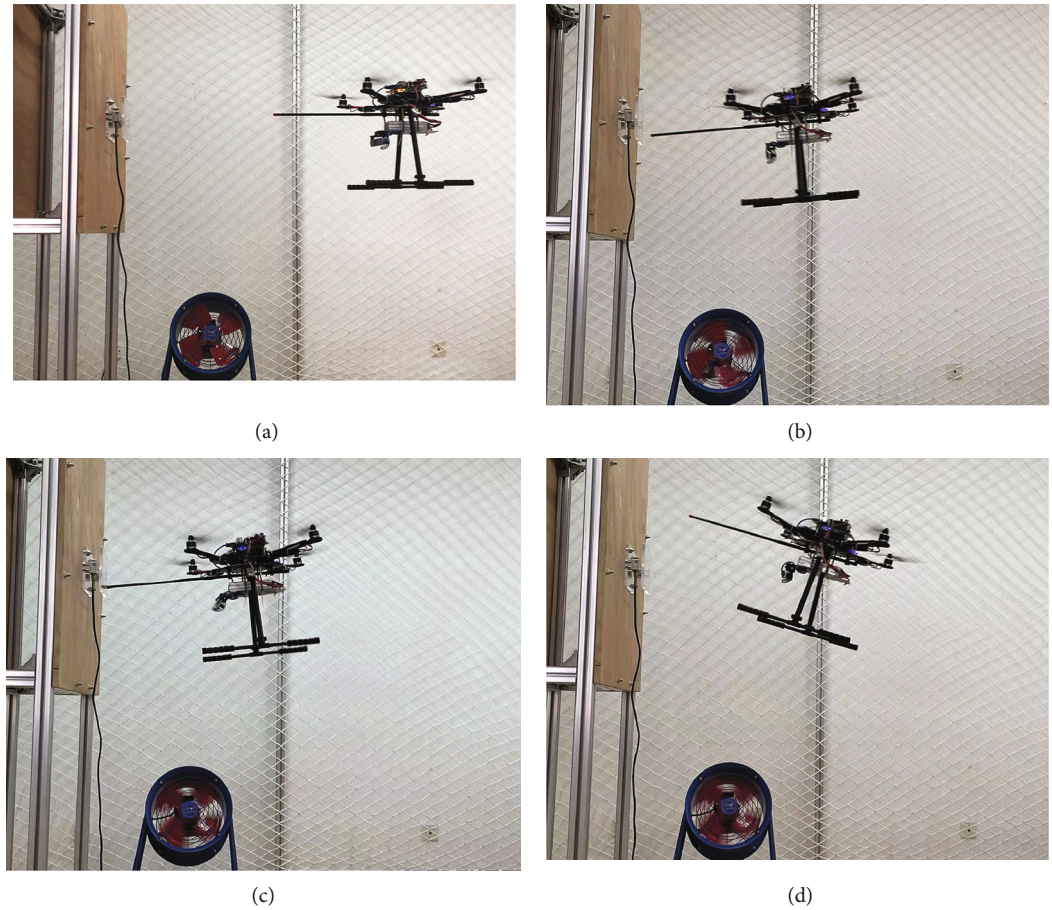

(a) (b) (c) (d)

Figure 12: The process of flight experiments: (a) approaching; (b) contact transition; (c) contact control; (d) return.

neither the force nor the position convergence. Moreover, although we do not propose the evaluation criteria for the extended state observer, it can be judged that the extended state observer has excellent estimation and compensation abilities by comparing the CNGFTSM and GFTSM simulation results.

5. Flight Experiments

This section applies the designed controller to the developed aerial manipulator system for contact experiments to verify the proposed controller's performance and effectiveness.

5.1. Hardware Setup. As shown in Figure 11(a), we developed a contact force measurement system to measure and record the force information, which consists of a pressure sensor and a data acquisition card. The sensor used as the contact target of the aerial manipulator with a contact surface area of 20×20 cm is installed in the centre of an 80×80 cm wood board, and its contact centre is 1.35 m above the ground. The sampling rate of the data acquisition card is 200 sa/s. The system obtains the path information by the Intel T265 binocular camera. The attitude data is obtained from the inertial measurement unit (IMU) with a measurement accuracy of ±0.03 rad. The inertial coordinate system definition is shown in Figure 11(b): the origin of the coordinates is O. The direction perpendicular to the board surface and pointing to the board surface is the positive direction of the x-axis. The y-z plane is parallel to the board surface.

As shown in Figure 12, the experimental process is divided into four stages: approach, contact transition, contact force control, and return. The aerial manipulator takes off at $[-0.5\,\text{m}, 0\,\text{m}, 0\,\text{m}]$ and touches the pressure sensor at $[-0.2\,\text{m}, 0\,\text{m}, 1.35\,\text{m}]$. We place a fan at the lower right of the contact position to add external disturbances to the system in which the disturbances are two levels, the fan's first and second gear winds.

Figures 13–15 show the experimental results of the contact force control of the aerial manipulator. In Figures 13(b) and 13(c), Y+ESO and Z+ESO represent the experimental results of the controller with an extended state observer, while Y and Z are without the ESO's results. We can know that the system position error with an ESO has a higher precision than the result without an ESO.

Figures 14(a) and 14(b) show the result of the pitch angle and the contact force, respectively. Figure 14(c) shows the errors for F and F_d, F_{mes}, and F_d. Obviously, the error between the measured and expected values is more significant due to the system's vibration causing the sensor's vibration to increase the measurement error. Therefore, the calculated value by the pitch angle is more precise.

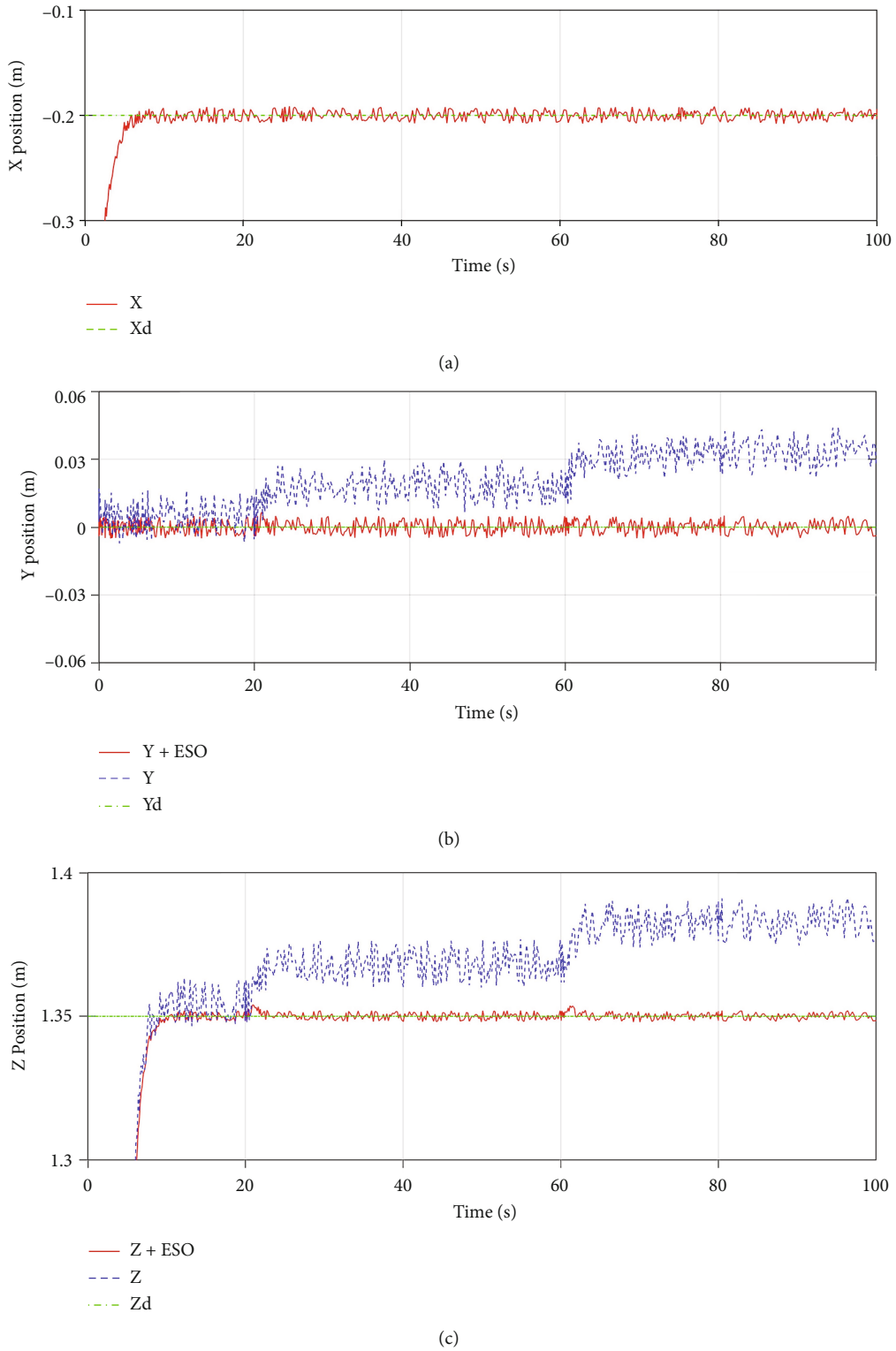

Figure 13: The position results of experiments. (a) Position changes in the x-axis direction. (b) Position changes in the y-axis direction. (c) Position changes in the z-axis direction.

Figure 15 shows the estimation result of the disturbance from the extended state observer. Although the actual disturbances are not measured, we can judge from the experimental results that the designed extended state observer has better tracking interference performance. Hence, the above results demonstrate that the proposed controller can validly guarantee the aerial manipulator's steady contact with the environment when influenced by external wind.

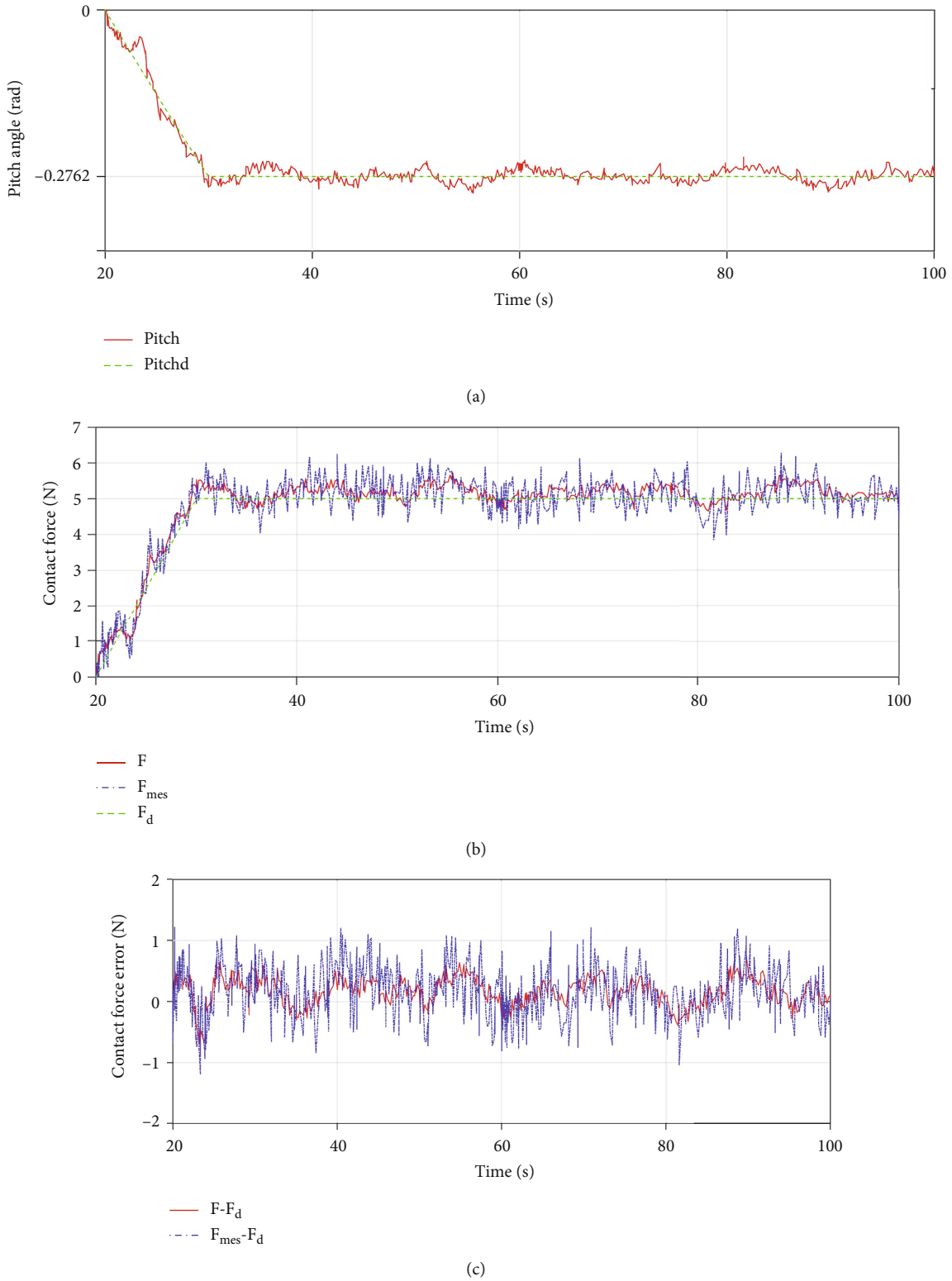

FIGURE 14: (a) The pitch angle results of experiments. (b) The contact force results. F represents the value obtained by the pitch angle calculation; F_{mes} represents the measurement of the sensor; F_d represents the expected value. (c) The contact force errors.

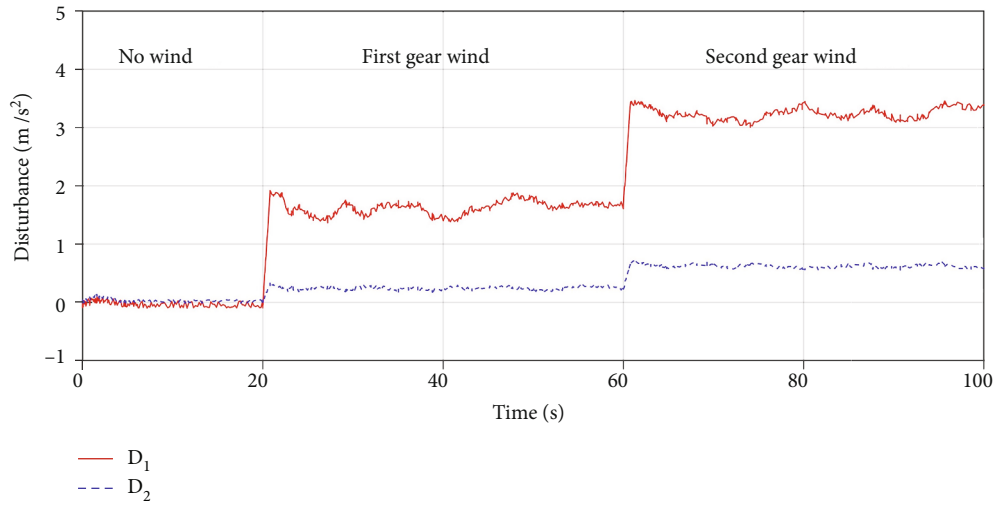

FIGURE 15: The estimation value of the external disturbances. D_1 and D_1 are the estimated values in the position and attitude systems, respectively.

6. Conclusion

In this paper, the dynamics model of the aerial manipulator is analyzed and modelled, where the unmeasured internal interaction generated by the coupling effect and the random environmental disturbances are considered simultaneously. We propose a composite controller combined with the extended state observer and the nonsingular global fast terminal sliding mode algorithm for the aerial manipulator to conduct contact tasks under the influence of disturbances, where the state observer is used to estimate and compensate for uncertainties and external disturbances. Several contact force tracking simulations are carried out to evaluate the capabilities of the proposed controller. The results show that the controller effectively enhances the closed-loop system's convergence and antidisturbance capability compared with the other controllers, which ensures that the aerial manipulator can stably contact the environment when affected by external disturbances. In addition, the proposed sliding mode can guarantee good response dynamics, which has low structural complexity and the amount of calculation. The final actual experiments verify the controller's performance and effectiveness.

In the future, we will pay more attention to the antidisturbance control of the aerial manipulator. Meanwhile, we will also expand the degree of freedom of the manipulator and conduct aerial tasks.

Abbreviations

UAV: Unmanned aerial vehicle
ESO: Extended state observer
CNGFTSM: Composite nonsingular global fast terminal sliding mode
GFTSM: Nonsingular global fast terminal sliding mode
CNSM: Composite nonsingular sliding mode
CPID: Composite proportional integral derivative
IBC: Integral backstepping control
IMU: Inertial measurement unit.

Data Availability

The data used to support the findings of this study are included within the article.

Conflicts of Interest

The authors declare no conflict of interest.

Authors' Contributions

L.S. was responsible for the methodology; L.S. and Q.F. were responsible for the software; L.S., Q.F., and P.M. were in charge of the validation; L.S. was responsible for the data curation; L.S. was in charge of the original draft preparation; L.S. and J.W. were in charge of the review and editing; P.M. was in charge of visualization; and J.W. was in charge of supervision. All authors have read and agreed to the published version of the manuscript.

Acknowledgments

This research was funded by the Major Program for Science and Technology of Henan (Grant No. 181100110100) and Major Program for Science and Technology of Luoyang (Grant No. 2101018A).

References

[1] B. H. Alsalam, K. Morton, D. Campbell, and F. Gonzalez, "Autonomous UAV with vision based on-board decision making for remote sensing and precision agriculture," in *2017 IEEE Aerospace Conference*, Big Sky, MT, USA, 2017.

[2] J. Scherer, S. Yahyanejad, S. Hayat et al., "An autonomous multi-UAV system for search and rescue," in *Proceedings of the First Workshop on Micro Aerial Vehicle Networks, Systems, and Applications for Civilian Use*, Florence Italy, 2015.

[3] G. Lindner, K. Schraml, R. Mansberger, and J. Hübl, "UAV monitoring and documentation of a large landslide," *Applied Geomatics*, vol. 8, no. 1, pp. 1–11, 2016.

[4] D. Chowdhury, M. Sarkar, M. Z. Haider, S. A. Fattah, and C. Shahnaz, "Design and implementation of a cyber-vigilance system for anti-terrorist drives based on an unmanned aerial vehicular networking signal jammer for specific territorial security," in *2017 IEEE Region 10 Humanitarian Technology Conference (R10-HTC)*, Dhaka, Bangladesh, 2017.

[5] J. L. Scholten, M. Fumagalli, S. Stramigioli, and R. Carloni, "Interaction control of an UAV endowed with a manipulator," in *2013 IEEE International Conference on Robotics and Automation*, Karlsruhe, Germany, 2013.

[6] M. Á. Trujillo, J. Martínez-de Dios, C. Martín, A. Viguria, and A. Ollero, "Novel aerial manipulator for accurate and robust industrial NDT contact inspection: a new tool for the oil and gas inspection industry," *Sensors*, vol. 19, no. 6, p. 1305, 2019.

[7] Y. Sun, Z. Jing, P. Dong, J. Huang, W. Chen, and H. Leung, "A switchable unmanned aerial manipulator system for window-cleaning robot installation," *IEEE Robotics and Automation Letters*, vol. 6, no. 2, pp. 3483–3490, 2021.

[8] V. Lippiello and F. Ruggiero, "Cartesian impedance control of a UAV with a robotic arm," *IFAC Proceedings Volumes*, vol. 45, no. 22, pp. 704–709, 2012.

[9] F. Huber, K. Kondak, K. Krieger et al., "First analysis and experiments in aerial manipulation using fully actuated redundant robot arm," in *2013 IEEE/RSJ International Conference on Intelligent Robots and Systems*, Tokyo, Japan, 2013.

[10] H. Yang and D. Lee, "Dynamics and control of quadrotor with robotic manipulator," in *2014 IEEE International Conference on Robotics and Automation (ICRA)*, Hong Kong, China, 2014.

[11] M. Kobilarov, "Nonlinear trajectory control of multi-body aerial manipulators," *Journal of Intelligent and Robotic Systems*, vol. 73, no. 1-4, pp. 679–692, 2014.

[12] H. Seo, S. Kim, and H. Jin Kim, "Aerial grasping of cylindrical object using visual servoing based on stochastic model predictive control," in *2017 IEEE International Conference on Robotics and Automation (ICRA)*, Singapore, 2017.

[13] G. Garimella and M. Kobilarov, "Towards model-predictive control for aerial pick-and-place," in *2015 IEEE International Conference on Robotics and Automation (ICRA)*, Seattle, WA, USA, 2015.

[14] D. Lunni, A. Santamaria-Navarro, R. Rossi, P. Rocco, L. Bascetta, and J. Andrade-Cetto, "Nonlinear model predictive control for aerial manipulation," in *2017 International Conference on Unmanned Aircraft Systems (ICUAS)*, Miami, FL, USA, 2017.

[15] F. Caccavale, G. Giglio, G. Muscio, and F. Pierri, "Adaptive control for UAVs equipped with a robotic arm," *IFAC Proceedings Volumes*, vol. 47, no. 3, pp. 11049–11054, 2014.

[16] H. Lee and H. Jin Kim, "Estimation, control, and planning for autonomous aerial transportation," *IEEE Transactions on Industrial Electronics*, vol. 64, no. 4, pp. 3369–3379, 2017.

[17] F. Pierri, G. Muscio, and F. Caccavale, "An adaptive hierarchical control for aerial manipulators," *Robotica*, vol. 36, no. 10, pp. 1527–1550, 2018.

[18] C. Papachristos, K. Alexis, and A. Tzes, "Efficient force exertion for aerial robotic manipulation: exploiting the thrust-vectoring authority of a tri-tiltrotor UAV," in *2014 IEEE International Conference on Robotics and Automation (ICRA)*, Hong Kong, China, 2014.

[19] S. Kim, S. Choi, and H. Jin Kim, "Aerial manipulation using a quadrotor with a two DOF robotic arm," in *2013 IEEE/RSJ International Conference on Intelligent Robots and Systems*, Tokyo, Japan, 2013.

[20] M. Pouzesh and S. Mobayen, "Event-triggered fractional-order sliding mode control technique for stabilization of disturbed quadrotor unmanned aerial vehicles," *Aerospace Science and Technology*, vol. 121, article 107337, 2022.

[21] K. A. Alattas, O. Mofid, A. K. Alanazi et al., "Barrier function adaptive nonsingular terminal sliding mode control approach for quad-rotor unmanned aerial vehicles," *Sensors*, vol. 22, no. 3, p. 909, 2022.

[22] O. Mofid, S. Mobayen, and A. Fekih, "Adaptive integral-type terminal sliding mode control for unmanned aerial vehicle under model uncertainties and external disturbances," *IEEE Access*, vol. 9, pp. 53255–53265, 2021.

[23] M. Xiangdong, H. Yuqing, Z. Hongda, Y. Liying, G. Feng, and H. Jianda, "Contact force control of aerial manipulator systems," *Control Theory & Applications*, vol. 36, 2019.

[24] M. E. N. G. Xiangdong, H. E. Yuqing, and H. A. N. Jianda, "Hybrid force/position control of aerial manipulators in contact operation," *Robot*, vol. 42, no. 2, pp. 167–178, 2020.

[25] T. Ikeda, S. Yasui, M. Fujihara et al., "Wall contact by octo-rotor UAV with one DoF manipulator for bridge inspection," in *2017 IEEE/RSJ International Conference on Intelligent Robots and Systems (IROS)*, Vancouver, BC, Canada, 2017.

[26] H. C. Zhao, H. Q. Zhou, and S. H. Wang, "Sliding mode control of quad-rotor UAV based on extended state observer," *Command Control and Simulation*, vol. 42, no. 5, pp. 91–96, 2020.

[27] Z. Zhenhua, X. Liang, J. Bin, and C. Dong, "Fast nonsingular terminal sliding mode trajectory tracking control of a quadrotor UAV based on extended state observers," *Control & Decision*, vol. 37, no. 9, pp. 2201–2210, 2022.

[28] S. Li, J. Yang, W. H. Chen, and X. Chen, "Generalized extended state observer based control for systems with mismatched uncertainties," *IEEE Transactions on Industrial Electronics*, vol. 59, no. 12, pp. 4792–4802, 2011.

[29] L. Meier, P. Tanskanen, L. Heng, G. H. Lee, F. Fraundorfer, and M. Pollefeys, "PIXHAWK: a micro aerial vehicle design for autonomous flight using onboard computer vision," *Autonomous Robots*, vol. 33, no. 1-2, pp. 21–39, 2012.

[30] J. S. Gao, L. Y. Duan, and L. W. Deng, "Anti-interference trajectory tracking control of quadrotor UAV," *Control and Decision*, vol. 36, no. 2, pp. 379–386, 2021.

[31] A. Suarez, V. M. Vega, M. Fernandez, G. Heredia, and A. Ollero, "Benchmarks for aerial manipulation," *IEEE Robotics and Automation Letters*, vol. 5, no. 2, pp. 2650–2657, 2020.